NANO LETTERS

pubs.acs.org/NanoLett Letter

Chiral Third-Harmonic Metasurface for Multiplexed Holograms

Xuanmiao Hong, Kai Wang,* Chao Guan, Xiaobo Han, Yang Chen, Shuhang Qian, Xiangyuan Xing, Cheng-Wei Qiu,* and Peixiang Lu*

Cite This: https://doi.org/10.1021/acs.nanolett.2c02283 Read Online

ACCESS | Metrics & More | Article Recommendations | Supporting Information

ABSTRACT: Chiral nonlinear metasurfaces could natively synergize nonlinear wavefront manipulation and circular dichroism, offering enhanced capacity for multifunctional and multiplexed nonlinear metasurfaces. However, it is still quite challenging to simultaneously enable strong chiral response, precise wavefront control, high nonlinear conversion efficiency, and independent functions on spins and chirality. Here, we propose and experimentally demonstrate multiplexed third-harmonic (TH) holograms with four channels based on a chiral Au-ZnO hybrid metasurface. Specifically, the left- and right-handed circularly polarized (LCP and RCP) components of the TH holographic images can be designed independently under the excitation of an LCP (or RCP) fundamental beam. In addition, the TH conversion efficiency is measured to be as large as 10^{-5}, which is 8.6 times stronger than that of a bare ZnO film with the same thickness. Thus, our work provides a promising platform for realizing efficient and multifunctional nonlinear nanodevices.

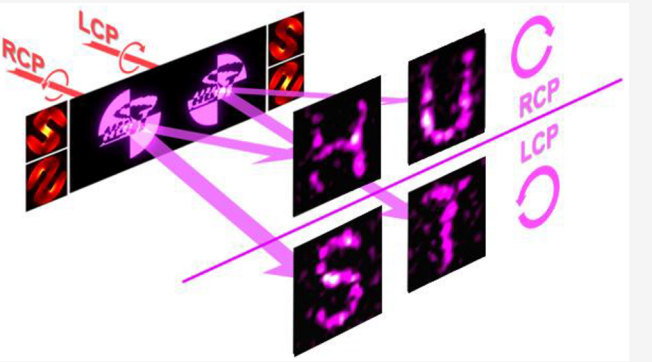

KEYWORDS: *chiral nonlinear metasurface, third-harmonic generation (THG), geometric phase control, multiplexed holograms, hybrid nanostructure*

The conversion of polarization in light−matter interactions is usually accompanied by a phase change, which is known as the Pancharatnam−Berry phase or geometric phase. As a realization, linear geometric metasurfaces have been extensively demonstrated for the wavefront shaping of light.[1−6] One important step to further exploit both copolarized and cross-polarized components is to extend geometric the metasurface into the nonlinear optics regime.[7,8] In the past few years, multifunctional nonlinear metasurfaces have been demonstrated, most of which are based on a nonlinear geometric phase.[9−20] For example, the copolarized and cross-polarized components of a third-harmonic (TH) beam carry geometric phases of 2φ and 4φ when pumped with circular polarization (CP) light. As a result, two pairs of geometric-phase distribution sets can be encoded for different polarizations of TH beams. As shown in Figure s1 in the Supporting Information, two independent geometric phases can be achieved with nonlinear metasurface, which is expressed by

$$\begin{bmatrix} E_R(3\omega) \\ E_L(3\omega) \end{bmatrix} \propto \mathbf{T} \begin{bmatrix} E_R^3(\omega) \\ E_L^3(\omega) \end{bmatrix} = \begin{bmatrix} T_{RR} & T_{RL} \\ T_{LR} & T_{LL} \end{bmatrix} \begin{bmatrix} E_R^3(\omega) \\ E_L^3(\omega) \end{bmatrix} = \begin{bmatrix} Ae^{i\cdot(2\varphi)} & Be^{i\cdot(-4\varphi)} \\ Be^{i\cdot(4\varphi)} & Ae^{i\cdot(-2\varphi)} \end{bmatrix} \begin{bmatrix} E_R^3(\omega) \\ E_L^3(\omega) \end{bmatrix} \quad (1)$$

where **T** is the nonlinear conversion matrix, the subscripts R and L represent right- and left-handed circular polarization (RCP and LCP), and A and B are the spin-dependent nonlinear conversion amplitudes, determined by the material and structure of the scatterer. It is observed that the elements T_{RR} and T_{LL} possess identical amplitude and opposite phases, as well as T_{RL} and T_{LR}. Therefore, the polarization-dependent property

Received: July 13, 2022
Revised: November 3, 2022

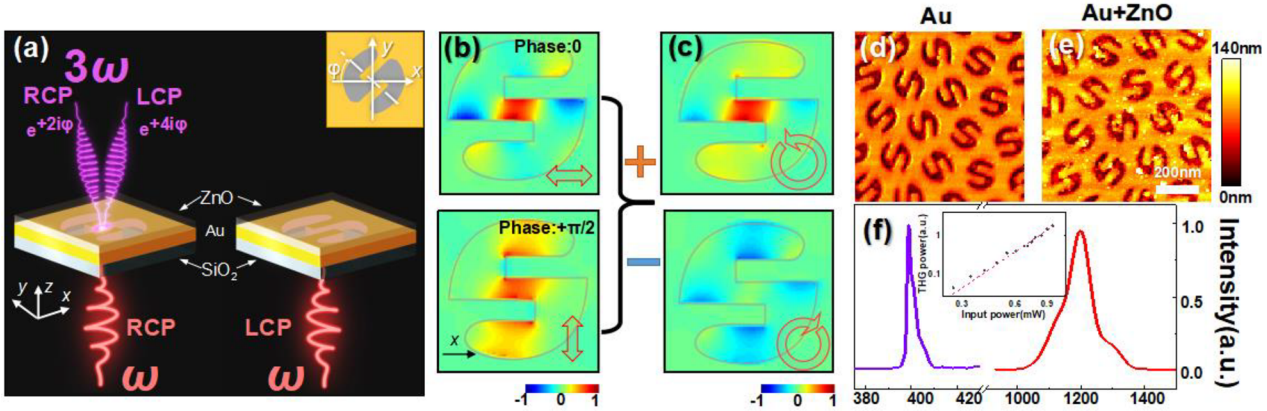

Figure 1. (a) Schematic illustration of the chiral responsive Au-ZnO nonlinear metasurface for TH wavefront modulation. The inset shows the shape of the Au nanohole. The diameter is 900 nm, and the arm width and the slit in the center are both150 nm. The thickness of the Au film is 60 nm, covered with a 50 nm thick ZnO layer. The sample is fabricated on a quartz substrate. (b) Calculated E_y distribution in a pixel of the Au-ZnO hybrid metasurfaces under LP excitation along the x axis and y axis. The phase difference between them is $\pi/2$. (c) Calculated E_y distribution in a pixel under the excitation of RCP and LCP light. (d, e) AFM images of the Au metasurface and the Au-ZnO hybrid metasurfaces, respectively. (f) Measured spectrum of the TH signal (at 400 nm) from Au-ZnO hybrid metasurfaces and the excitation light (at 1200 nm). The insert is the input−output dependence of the excitation power and TH intensity. Both axes are logarithms. The slope of the fitted line is 3.07.

has been locked by the intrinsic property of a nonlinear geometric phase.

To unleash the powerfulness of nonlinear geometric phases, chiral scatterers are adopted to enable the independent manipulation of a nonlinear geometric phase under different pump polarizations. Ideally, the R- and L-handed scatterers only respond to the RCP and LCP pump light, respectively. Then the nonlinear conversion matrices of the two enantiomer scatterers T_R and T_L can be expressed as

$$T_R = \begin{bmatrix} Ae^{i\cdot(2\varphi)} & 0 \\ Be^{i\cdot(4\varphi)} & 0 \end{bmatrix} \quad (2)$$

$$T_L = \begin{bmatrix} 0 & Be^{i\cdot(-4\theta)} \\ 0 & Ae^{i\cdot(-2\theta)} \end{bmatrix} \quad (3)$$

By arranging those two types of chiral scatterers with different orientation angles (φ and θ), four independent sets of geometric-phase distributions can be encoded in such a chiral nonlinear metasurface, as depicted in Figure s1c. Each set can be separately accessed by the different combinations of the pump and harmonic polarizations. Although chiral geometric metasurfaces have been frequently reported in the linear optics regime,[21−35] it is still challenging to extend them to the nonlinear regime. Many previous works have only realized the combination of nonlinear frequency conversion and chiral responses.[36−45] Recently, a pioneering work reported on a chiral nonlinear metasurface exhibiting phase control, which is based on a Trisceli- and Gammadion-type two-dimensional structure.[46] However, the demonstrated phase control is still quite elementary (beam steering).

In this work, we proposed and experimentally demonstrated a chiral nonlinear hybrid metasurface for TH wavefront modulation, which is composed of an Au nanohole array filled with ZnO film. It shows a strong chiral response to LCP and RCP light excitation, while precisely controlling the geometric phase of TH signals. It is demonstrated that the emitted TH signal can be controlled through four different channels simultaneously. For both LCP and RCP excitations, the LCP and RCP components of the TH holographic images can be manipulated independently. The CD coefficient is determined to be 0.38. In addition, the TH conversion efficiency is measured to be 10^{-5}, nearly 1 order of magnitude higher than that of the ZnO film with the same thickness. Therefore, it offers a promising platform to realize efficient and multifunctional nonlinear wavefront control.

Figure 1a illustrates a pixel of the chiral Au-ZnO hybrid metasurface. Specifically, it shows an S-shaped Au nanohole composed of a circular hole and two nanorods, which is designed to be on resonance with the fundamental wavelength at 1200 nm in experiments. The diameter of the nanohole is 900 nm, and the nanorod width and the slit in the center are both 150 nm. The period of the Au-ZnO metasurface is 1200 nm. The sample is fabricated on a quartz substrate, and the thickness of the Au film is 60 nm, loaded with a 50 nm thick ZnO layer. Importantly, the S-shaped unit can further be mirror-inversed, forming a chiral response to the same excitation of CP light. For example, under the excitation of RCP light, the S-shaped unit is activated while the inversed unit is forbidden, and *vice versa*. Furthermore, under RCP light excitation, there are two components of the emitted TH signal: an RCP-TH signal with a $+2\varphi$ phase factor and an LCP-TH signal with $+2\varphi$ phase factor, where φ is the rotation angle of the S-shaped Au nanohole. θ is the rotation angle of the inversed S-shaped Au nanohole.

Figure 1b,c illustrates the modulation principle of the Au-ZnO hybrid nonlinear metasurface. Figure 1b shows the calculated y component of the electric-field distribution in the S-shaped nanohole under a linearly polarized (LP) excitation (along the x or y axis), showing two resonance modes. It is worth noting that E_y is the dominant component and E_x is negligible in our work (see Figure s2). According to the simple harmonic oscillator model, the resonant mode under x-polarized light excitation has a longer phase delay than that under y-polarized light excitation. Then, a phase delay of $\pi/2$ between two resonant modes can be achieved by adjusting the size of the S-shaped nanohole. Under a CP light excitation, both resonant modes are excited simultaneously, introducing an additional phase delay of $\pi/2$ or $-\pi/2$. Therefore, the phase delay between two resonant modes will be 0 or π under RCP or LCP light excitation, respectively. Figure 1c shows the calculated E_y in the S-shaped

https://doi.org/10.1021/acs.nanolett.2c02283
Nano Lett. XXXX, XXX, XXX−XXX

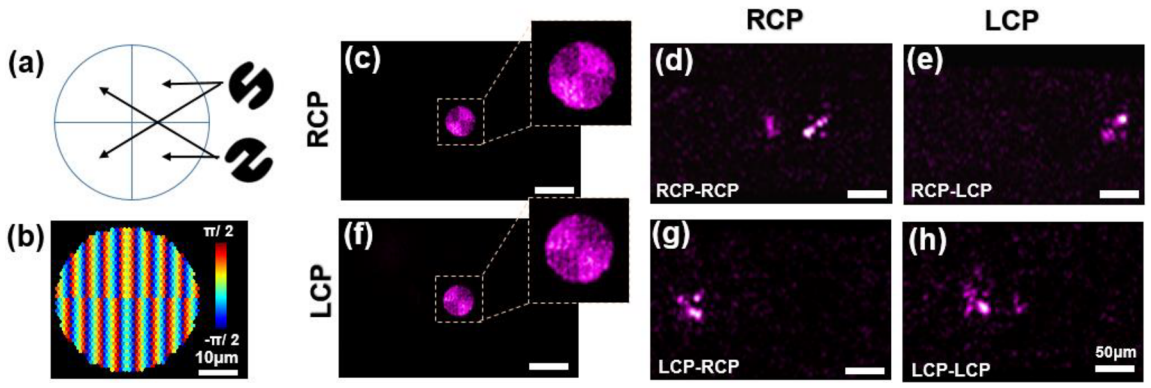

Figure 2. (a) S-shaped Au-ZnO nanoholes (RCP responsive) are in the 1 and 3 quadrants and inversed S-shaped Au-ZnO nanoholes (LCP responsive) are in the 2 and 4 quadrants. (b) TH phase distribution of TH signal with $+2\varphi$ and $+4\varphi$ phase factors at the Au-ZnO hybrid metasurfaces. (c, f) TH intensity distribution on the sample surface under RCP and LCP excitation. (d, e, g, h) Different components of the TH signal at 600 μm under RCP and LCP excitation. Note that, the LCP component of the TH signal under RCP excitation is labeled RCP-LCP.

nanohole under a CP light excitation, indicating a clear spin-dependent distribution. This can be regarded as the addition or subtraction of the two modes in Figure 1c. Furthermore, both Figure 1c and Figure s3 show that the electric field is concentrated in the center with the polarization perpendicular to the slit (under RCP excitation). Under the LCP light excitation, the electric field is distributed in the edge of the nanohole, leading to a chiral response to the CP fundamental beam.

In experiments, a filled ZnO film acts as a nonlinear material and no TH signal can be observed in the bare S-shaped Au nanohole under the same excitation condition. Compared with previous works,[47−49] an S-shaped Au nanohole with a much larger gap (~150 nm) is used in our work for filling the ZnO film. While it inevitably lowers the peak intensity of the local field inside the Au nanoholes, it obviously increases the overlap region between its local field and the filled ZnO film. Since the ZnO film is polycrystalline, it can be regarded to be isotropic, whose TH susceptibility is written as $\chi^{(3)}_{xxxx} = \chi^{(3)}_{xxyy} = \chi^{(3)}_{xyxy} = \chi^{(3)}_{xyyx} = \chi^{(3)}$. Then, based on the nonlinear scattering theory,[50,51] the TH conversion matrix of a unit-cell nanostructure is calculated as

$$T_{R-} = \begin{bmatrix} 5.48e^{i\cdot(2\varphi)} & 3.67e^{i\cdot(-4\varphi)} \\ 6.66e^{i\cdot(4\varphi)} & 3.31e^{i\cdot(-2\varphi)} \end{bmatrix} \quad (4)$$

$$T_{L-} = \begin{bmatrix} 3.31e^{i\cdot(2\theta)} & 6.66e^{i\cdot(-4\theta)} \\ 3.67e^{i\cdot(4\theta)} & 5.48e^{i\cdot(-2\theta)} \end{bmatrix} \quad (5)$$

The calculated distribution of TH intensity is shown in Figure s3b. The CD coefficient is defined as $(I^{3\omega}_{RCP} - I^{3\omega}_{LCP})/(I^{3\omega}_{RCP} + I^{3\omega}_{LCP})$, where $I^{3\omega}_{RCP}$ and $I^{3\omega}_{LCP}$ are the total TH intensities under RCP and LCP excitation, respectively. The calculated CD is 50% (see the Supporting Information for further details). In addition, we have

$$\frac{E_x(3\omega)}{E_y(3\omega)} = \frac{E_x(\omega)}{E_y(\omega)} \quad (6)$$

This indicates that the polarization of the TH signal is the same as that of the fundamental beam. Under a specific CP light excitation, the polarization direction of the emitted TH signal is always perpendicular to the slit of each unit. It results in two CP components of TH signals, carrying the phase factors of $+2\varphi$ and $+4\varphi$ for the copolarized and cross-polarized components, respectively. Although the coupling effect between the Au nanoholes may lead to fluctuations of the TH intensity, the phase delay of the TH signal agrees with the theoretical results (see Figure s4 for further discussions).

The S-shaped Au nanohole is fabricated by focused ion beam (FIB) etching, and the ZnO film is deposited by magnetron sputtering. Figure 1d,e shows the typical atomic force microscope (AFM) images before and after ZnO film deposition, respectively (and the SEM image is shown in Figure s5). The thickness of the ZnO film is measured to be ~50 nm. It is observed that the surface morphologies are quite similar, indicating that ZnO is well loaded into the Au nanohole array. Figure 1f shows the measured spectrum of the fundamental beam and TH signal, and the inset gives the input−output curve. After the coordinates are logarithmic, the slope of the fitted line is 3.07, which is consistent with the theory. We evaluate the TH signal power of the sample by comparing it with a 50 nm thick ZnO film. The power density of the TH signal of the sample is 8.6 times larger than that of the ZnO film, and then the TH conversion efficiency is estimated to be 10^{-5} under 1 mW excitation power.

A sample was used to test the chirality and phase modulation of the Au-ZnO nonlinear metasurface. Figure 2a illustrates the distribution of unit types. S-shaped Au-ZnO hybrids are distributed in the first and the third quadrants, while the inverted *S*-shaped hybrids are located at the second and the fourth quadrants. Figure 2b shows the target phase distribution of the emitted TH signals on the sample surface. It indicates a gradient phase variation along the x axis, leading to 5 and 10° deflections for the component of the TH signal with $+2\varphi$ and $+4\varphi$ phase factors, respectively. Figure 2c,f presents the measured TH intensity distribution on the sample surface (z = 0 μm) under the excitation of RCP and LCP light, respectively. Clearly, the TH intensities are different in different quadrants, which can be switched on/off by CPL excitation. The CD coefficient of the TH signal is measured to be 0.38, which is less than the theoretical value. This is attributed to the irregular nanostructures of the ZnO film in the Au-ZnO hybrids caused by processing, leading to an unexpected TH background that lower the CD coefficient (see Figure s6). However, most of these background TH signals do not carry any phase information, which are randomly and uniformly scattered into the space without causing the quality degradation of holographic imaging. Furthermore, Figure 2d,e presents the RCP and LCP components of emitted TH signals (at z = 600 μm) under the

https://doi.org/10.1021/acs.nanolett.2c02283
Nano Lett. XXXX, XXX, XXX−XXX

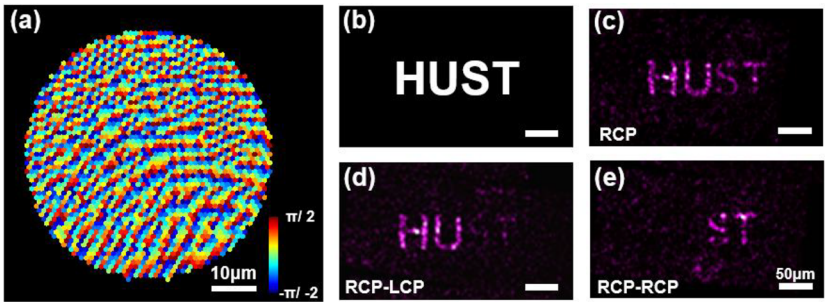

Figure 3. (a) TH phase distribution at the Au-ZnO hybrid metasurfaces. The target holographic images are measured at 600 μm from the sample. (b) The target hologram image. The pattern "HU" is the LCP component, and the pattern "ST" is the RCP component. (c–e) Measured holographic images: (c) total TH signals; (d, e) RCP/LCP components of TH signals.

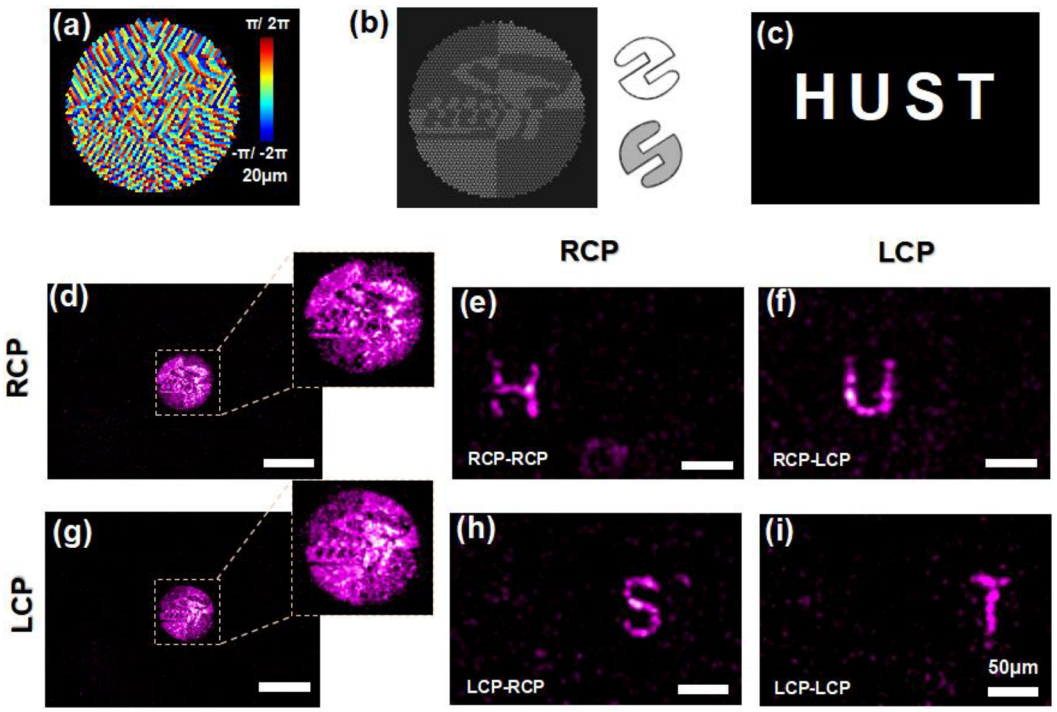

Figure 4. (a) TH phase distribution at the Au-ZnO hybrid metasurfaces. (b) Illustration of the metasurfaces. The S-shaped Au-ZnO nanoholes (RCP responsive) are in the white area, and the inversed S-shaped Au-ZnO nanoholes (LCP responsive) are in the gray area. (c) Target images of holograms. "H", "U", "S", and "T" correspond to the combinations of the polarization of the excitation and TH signals. (d, g) Measured TH signal distributions on the sample surface under RCP and LCP excitation. (e, f, h, i) Different components of the TH hologram signal under RCP and LCP excitation. The LCP component of the TH signal under RCP excitation is labeled RCP-LCP.

excitation of RCP light, respectively. The deflected angle of the RCP TH component is determined to be 5°, which is half of that of the LCP TH component (10°). Since the RCP and LCP TH components carry phase factors of $+2\varphi$ and $+4\varphi$ in principle, the experimental results show a good agreement with the theory. Figure 2g,h presents the RCP and LCP components of emitted TH signals (at z = 600 μm) under LCP light excitation, which are related to Figure 2e,d, respectively. In addition, it is observed that some weak TH signals are propagated without deflection, which may be ascribed to the structural errors. More detailed information can be found in Supporting Information.

The four-channel control of the TH signal is further demonstrated. Figure 3a shows the phase distribution of the TH signal on the sample surface. The holographic imaging plane is designed to be 600 μm away from the sample (z = 600 μm). Since all the pixels are S-shaped Au nanoholes, it is switched on/off under RCP/LCP light excitation, respectively. Figure 3b illustrates the target pattern "HUST", which is the short form of "*Huazhong University of Science and Technology*". Specifically, the "HU" pattern is an LCP component with a phase factor of $+4\varphi$, while the "ST" pattern is an RCP component with a phase factor of $+2\varphi$. It is worth noting that the position of the holographic image is designed to be slightly off-axis to avoid the influence of the background TH signal. Figure 3c presents the total TH intensity distribution, while Figure 3d,e gives the extracted LCP and RCP components of emitted TH signals, respectively. It is in good agreement with the theoretical designs. One can see that the intensity of the RCP component ("ST") of the holographic image is weaker than that of the LCP component ("HU"). This is because, under the excitation of RCP light, the electric field in the center slit of the Au nanohole has larger LCP components, which can be corrected by considering the different weights of both components in the design. As the excitation polarization is changed to LCP, the S-shaped pixels of the Au-ZnO metasurface

https://doi.org/10.1021/acs.nanolett.2c02283
Nano Lett. XXXX, XXX, XXX−XXX

are switched off. Hence, there are no holographic images on both sides of the sample and only background noises can be observed.

Figure 4a shows the designed TH phase distribution of the sample. Under the excitation of the LCP (or RCP) fundamental beam, LCP and RCP components of the TH holographic images can be designed independently. Figure 4b shows the arrangement of normal and reversed S-shaped units. Under the excitation of a specific CP light, only one type of the unit can be switched on, resulting in a TH intensity pattern on the sample surface. Furthermore, the TH pattern is divided into four regions, and the adjacent regions are inverted to ensure that the areas of normal and inversed S-shaped units are equal for any patterns. Figure 4c illustrates the target pattern. The four-letter pattern corresponds to the different polarizations of the excitation light and the emitted TH signals, which can be regarded as four information channels. Under RCP light excitation, the pattern "HU" is observed. Specifically, the pattern "H" is the CP component of the TH signal, while the pattern "U" is the LCP component. Under LCP excitation, the pattern "ST" is observed. The pattern "S" is the RCP component, while the pattern "T" is the LCP component. The intensity of the holographic image can further be improved by correcting the intensity difference between the RCP and LCP components of the TH signal in each unit. Figure 4d,g presents the imaging on the sample surface under RCP and LCP light excitation, respectively. Complementary images are generated separately. Figure 4e,f,h,I shows the holographic images from four channels. The image intensity remains the same after precorrection. The pattern of the additional channel is independently controllable, so that this metasurface can carry more information. In the future, the TH conversion efficiency of the hybrid nonlinear metasurface could be further enhanced by replacing the ZnO with other efficient nonlinear materials. The CD coefficient could be improved by filling nonlinear materials only into the slit with an advanced processing technique, and the pixel density could also be improved because the coupling effects between units are significantly attenuated. Also, the CD coefficient might be improved by a purposely designed SPP coupling mode.[52]

In conclusion, we proposed and experimentally demonstrated multiplexed TH holograms with four channels based on a chiral Au-ZnO hybrid metasurface. Under the excitation of an LCP (or RCP) fundamental beam, LCP and RCP components of the TH holographic images can be designed independently. Furthermore, the TH signal from each pixel of the Au-ZnO metasurface can be switched on (or off) under LCP (or RCP) excitation, forming a specific TH intensity pattern on the sample surface. The result indicates that the CD coefficient of circular dichroism is 0.38 and the TH conversion efficiency is estimated to be 10^{-5}, which is 8.6 times larger than that of a ZnO film of the same thickness. This new type of nonlinear hybrid metasurface, combining precise phase control, circular dichroism, and an enhanced nonlinear conversion efficiency, provides a promising platform to realize efficient and multifunctional nonlinear wavefront control.

■ ASSOCIATED CONTENT

Supporting Information

The Supporting Information is available free of charge at https://pubs.acs.org/doi/10.1021/acs.nanolett.2c02283.

Mechanism of the metasurface, electric-field E_x and E_y distribution in the metasurface, details on the simulation result of multiple units and the effect of an irregular S-shaped structure, calculation of TH amplitude, phase distribution, and deflection angle, and optical measurement system (PDF)

■ AUTHOR INFORMATION

Corresponding Authors

Kai Wang − *Wuhan National Laboratory for Optoelectronics and School of Physics, Huazhong University of Science and Technology, Wuhan 430074, People's Republic of China;* orcid.org/0000-0003-2122-1294; Email: kale_wong@hust.edu.cn

Cheng-Wei Qiu − *Department of Electrical and Computer Engineering, National University of Singapore, Singapore 117583, Singapore*; Email: chengwei.qiu@nus.edu.sg

Peixiang Lu − *Wuhan National Laboratory for Optoelectronics and School of Physics, Huazhong University of Science and Technology, Wuhan 430074, People's Republic of China; Hubei Key Laboratory of Optical Information and Pattern Recognition, Wuhan Institute of Technology, Wuhan 430205, People's Republic of China; CAS Center for Excellence in Ultra-intense Laser Science, Shanghai 201800, People's Republic of China*; Email: lupeixiang@hust.edu.cn

Authors

Xuanmiao Hong − *Wuhan National Laboratory for Optoelectronics and School of Physics, Huazhong University of Science and Technology, Wuhan 430074, People's Republic of China*

Chao Guan − *Wuhan National Laboratory for Optoelectronics and School of Physics, Huazhong University of Science and Technology, Wuhan 430074, People's Republic of China*

Xiaobo Han − *Hubei Key Laboratory of Optical Information and Pattern Recognition, Wuhan Institute of Technology, Wuhan 430205, People's Republic of China*

Yang Chen − *CAS Key Laboratory of Mechanical Behavior and Design of Materials, Department of Precision Machinery and Precision Instrumentation, University of Science and Technology of China, 230027 Hefei, People's Republic of China;* orcid.org/0000-0002-8501-5417

Shuhang Qian − *Wuhan National Laboratory for Optoelectronics and School of Physics, Huazhong University of Science and Technology, Wuhan 430074, People's Republic of China*

Xiangyuan Xing − *Wuhan National Laboratory for Optoelectronics and School of Physics, Huazhong University of Science and Technology, Wuhan 430074, People's Republic of China*

Complete contact information is available at: https://pubs.acs.org/10.1021/acs.nanolett.2c02283

Author Contributions

K.W., C.-W.Q., and P.L. conceived and supervised the project. C.G., X.H., X.H., S.Q., and X.X. designed the experiments. All authors discussed the results. X.H., Y.C., and K.W. drafted the paper with the inputs from all authors.

Notes

The authors declare no competing financial interest.

https://doi.org/10.1021/acs.nanolett.2c02283
Nano Lett. XXXX, XXX, XXX−XXX

■ ACKNOWLEDGMENTS

This work was supported by the National Natural Science Foundation of China (Nos. 12274157, 12274334, 91850113, 11774115, 11904271, and 12021004), the 973 Programs under grant 2014CB921301, the Basic and Applied Basic Research Major Program of Guangdong Province (No. 2019B030302003). C.-W.Q. is supported by a grant (R-261-518-004-720) from the Advanced Research and Technology Innovation Centre (ARTIC), from the National University of Singapore. Y.C. acknowledges start-up funding from the University of Science and Technology of China. Special thanks are given to the Analytical and Testing Center of HUST and the Center of Micro-Fabrication and Characterization (CMFC) of WNLO for use of their facilities.

■ REFERENCES

(1) Stav, T.; Faerman, A.; Maguid, E.; Oren, D.; Kleiner, V.; Hasman, E.; Segev, M. Quantum entanglement of the spin and orbital angular momentum of photons using metamaterials. *Science* **2018**, *361* (6407), 1101−1103.

(2) Devlin, R. C.; Ambrosio, A.; Rubin, N. A.; Mueller, J. P. B.; Capasso, F. Arbitrary spin-to-orbital angular momentum conversion of light. *Science* **2017**, *358* (6365), 896−900.

(3) Luo, W.; Sun, S.; Xu, H.-X.; He, Q.; Zhou, L. Transmissive Ultrathin Pancharatnam-Berry Metasurfaces with nearly 100% Efficiency. *Physical Review Applied* **2017**, *7* (4), 044033.

(4) Huang, L.; Chen, X.; Muhlenbernd, H.; Li, G.; Bai, B.; Tan, Q.; Jin, G.; Zentgraf, T.; Zhang, S. Dispersionless phase discontinuities for controlling light propagation. *Nano Lett.* **2012**, *12* (11), 5750.

(5) Xiong, J.; Wu, S. Planar liquid crystal polarization optics for augmented reality and virtual reality: from fundamentals to applications. *eLight* **2021**, *1*, 3.

(6) Chen, Z.; Segev, M. Highlighting photonics: looking into the next decade. *eLight* **2021**, *1*, 2.

(7) Krasnok, A.; Tymchenko, M.; Alu, A. Nonlinear metasurfaces: a paradigm shift in nonlinear optics. *Mater. Today* **2018**, *21* (1), 8−12.

(8) Sain, B.; Meier, C.; Zentgraf, T. Nonlinear optics in all-dielectric nanoantennas and metasurfaces: a review. *Advanced Photonics* **2019**, *1* (2), 024002.

(9) Chen, Y.; Yang, X.; Gao, J. Spin-Selective Second-Harmonic Vortex Beam Generation with Babinet-Inverted Plasmonic Metasurfaces. *Advanced Optical Materials* **2018**, *6* (19), 1800646.

(10) Li, G.; Wu, L.; Li, K. F.; Chen, S.; Schlickriede, C.; Xu, Z.; Huang, S.; Li, W. D.; Liu, Y. J.; Pun, E. Y.; et al. Nonlinear Metasurface for Simultaneous Control of Spin and Orbital Angular Momentum in Second Harmonic Generation. *Nano Lett.* **2017**, *17* (12), 7974−7979.

(11) Bar-David, J.; Levy, U. Nonlinear Diffraction in Asymmetric Dielectric Metasurfaces. *Nano Lett.* **2019**, *19* (2), 1044−1051.

(12) Li, G.; Wu, L.; Li, K. F.; Chen, S.; Schlickriede, C.; Xu, Z.; Huang, S.; Li, W.; Liu, Y.; Pun, E. Y. B.; Zentgraf, T.; Cheah, K. W.; Luo, Y.; Zhang, S. Nonlinear Metasurface for Simultaneous Control of Spin and Orbital Angular Momentum in Second Harmonic Generation. *Nano Lett.* **2017**, *17* (12), 7974−7979.

(13) Nookala, N.; Lee, J.; Tymchenko, M.; Sebastian Gomez-Diaz, J.; Demmerle, F.; Boehm, G.; Lai, K.; Shvets, G.; Amann, M.-C.; Alu, A.; Belkin, M. Ultrathin gradient nonlinear metasurface with a giant nonlinear response. *Optica* **2016**, *3* (3), 283.

(14) Li, G. X.; Chen, S. M.; Pholchai, N.; Reineke, B.; Wong, P. W. H.; Pun, E. Y. B.; Cheah, K. W.; Zentgraf, T.; Zhang, S. Continuous control of the nonlinearity phase for harmonic generations. *Nat. Mater.* **2015**, *14* (6), 607−612.

(15) Mao, N.; Deng, J.; Zhang, X.; Tang, Y.; Jin, M.; Li, Y.; Liu, X.; Li, K.; Cao, T.; Cheah, K.; Wang, H.; Ng, J.; Li, G. Nonlinear Diatomic Metasurface for Real and Fourier Space Image Encoding. *Nano Lett.* **2020**, *20* (10), 7463−7468.

(16) Reineke, B.; Sain, B.; Zhao, R. Z.; Carletti, L.; Liu, B. Y.; Huang, L. L.; De Angelis, C.; Zentgraf, T. Silicon Metasurfaces for Third Harmonic Geometric Phase Manipulation and Multiplexed Holography. *Nano Lett.* **2019**, *19* (9), 6585−6591.

(17) Ye, W. M.; Zeuner, F.; Li, X.; Reineke, B.; He, S.; Qiu, C. W.; Liu, J.; Wang, Y. T.; Zhang, S.; Zentgraf, T. Spin and wavelength multiplexed nonlinear metasurface holography. *Nat. Commun.* **2016**, *7*, 7.

(18) Zhao, W.; Wang, K.; Hong, X.; Wang, B.; Lu, P.; et al. Large second-harmonic vortex beam generation with quasi-nonlinear spin-orbit interaction. *Science Bulletin* **2021**, *66*, 449−456.

(19) Hong, X.; Hu, G.; Zhao, W.; Wang, K.; Sun, S.; Zhu, R.; Wu, J.; Liu, W.; Loh, K. P.; Wee, A. T. S.; Wang, B.; Alu, A.; Qiu, C.-W.; Lu, P. Structuring Nonlinear Wavefront Emitted from Monolayer Transition-Metal Dichalcogenides. *Research* **2020**, *2020*, 9085782.

(20) Hu, G. W.; Hong, X. M.; Wang, K.; Wu, J.; Xu, H. X.; Zhao, W. C.; Liu, W. W.; Zhang, S.; Garcia-Vidal, F.; Wang, B.; Lu, P. X.; Qiu, C. W. Coherent steering of nonlinear chiral valley photons with a synthetic Au-WS2 metasurface. *Nat. Photonics* **2019**, *13* (7), 467−472.

(21) Yang, S. Y.; Liu, Z.; Yang, H. F.; Jin, A. Z.; Zhang, S.; Li, J. J.; Gu, C. Z. Intrinsic Chirality and Multispectral Spin-Selective Transmission in Folded Eta-Shaped Metamaterials. *Advanced Optical Materials* **2020**, *8* (4), 2070014.

(22) Ouyang, L. X.; Rosenmann, D.; Czaplewski, D. A.; Gao, J.; Yang, X. D. Broadband infrared circular dichroism in chiral metasurface absorbers. *Nanotechnology* **2020**, *31* (29), 295203.

(23) Liu, Z. G.; Xu, Y.; Ji, C. Y.; Chen, S. S.; Li, X. P.; Zhang, X. D.; Yao, Y. G.; Li, J. F. Fano-Enhanced Circular Dichroism in Deformable Stereo Metasurfaces. *Adv. Mater.* **2020**, *32* (8), 1907077.

(24) Yin, S. T.; Ji, W.; Xiao, D.; Li, Y.; Li, K.; Yin, Z.; Jiang, S. Z.; Shao, L. Y.; Luo, D.; Liu, Y. J. Intrinsically or extrinsically reconfigurable chirality in plasmonic chiral metasurfaces. *Opt. Commun.* **2019**, *448*, 10−14.

(25) Yang, S. Y.; Liu, Z.; Hu, S.; Jin, A. Z.; Yang, H. F.; Zhang, S.; Li, J. J.; Gu, C. Z. Spin-Selective Transmission in Chiral Folded Metasurfaces. *Nano Lett.* **2019**, *19* (6), 3432−3439.

(26) Wang, Z.; Wang, Y.; Adamo, G.; Teng, J. H.; Sun, H. D. Induced Optical Chirality and Circularly Polarized Emission from Achiral CdSe/ZnS Quantum Dots via Resonantly Coupling with Plasmonic Chiral Metasurfaces. *Laser Photon. Rev.* **2019**, *13* (3), 1800276.

(27) Tseng, M. L.; Lin, Z. H.; Kuo, H. Y.; Huang, T. T.; Huang, Y. T.; Chung, T. L.; Chu, C. H.; Huang, J. S.; Tsai, D. P. Stress-Induced 3D Chiral Fractal Metasurface for Enhanced and Stabilized Broadband Near-Field Optical Chirality. *Advanced Optical Materials* **2019**, *7* (15), 1900617.

(28) Zhu, A. Y.; Chen, W. T.; Zaidi, A.; Huang, Y. W.; Khorasaninejad, M.; Sanjeev, V.; Qiu, C. W.; Capasso, F. Giant intrinsic chiro-optical activity in planar dielectric nanostructures. *Light-Sci. Appl.* **2018**, *7*, 17158.

(29) Hu, J. P.; Zhao, X. N.; Lin, Y.; Zhu, A. J.; Zhu, X. J.; Guo, P. J.; Cao, B.; Wang, C. H. All-dielectric metasurface circular dichroism waveplate. *Sci. Rep-Uk* **2017**, *7*, 9.

(30) Zu, S.; Bao, Y.; Fang, Z. Planar plasmonic chiral nanostructures. *Nanoscale* **2016**, *8* (7), 3900−5.

(31) Wang, Q.; Plum, E.; Yang, Q. L.; Zhang, X. Q.; Xu, Q.; Xu, Y. H.; Han, J. G.; Zhang, W. L. Reflective chiral meta-holography: multiplexing holograms for circularly polarized waves. *Light-Sci. Appl.* **2018**, *7*, 9.

(32) Li, J. X.; Kamin, S.; Zheng, G. X.; Neubrech, F.; Zhang, S.; Liu, N. Addressable metasurfaces for dynamic holography and optical information encryption. *Sci. Adv.* **2018**, *4* (6), 7.

(33) Chen, Y.; Yang, X. D.; Gao, J. Spin-controlled wavefront shaping with plasmonic chiral geometric metasurfaces. *Light-Sci. Appl.* **2018**, *7*, 10.

(34) Chen, Y.; Yang, X. D.; Gao, J. 3D Janus plasmonic helical nanoapertures for polarization-encrypted data storage. *Light-Sci. Appl.* **2019**, *8*, 9.

(35) Chen, Y.; Gao, J.; Yang, X. D. Chiral Grayscale Imaging with Plasmonic Metasurfaces of Stepped Nanoapertures. *Advanced Optical Materials* **2019**, *7* (6), 1801467.

https://doi.org/10.1021/acs.nanolett.2c02283
Nano Lett. XXXX, XXX, XXX−XXX

(36) Tang, Y.; Liu, Z.; Deng, J.; Li, K.; Li, J.; Li, G. Nano-Kirigami Metasurface with Giant Nonlinear Optical Circular Dichroism. *Laser Photon. Rev.* **2020**, *14* (7), 2000085.
(37) Ohnoutek, L.; Cho, N. H.; Murphy, A. W. A.; Kim, H.; Rasadean, D. M.; Pantos, G. D.; Nam, K. T.; Valev, V. K. Single Nanoparticle Chiroptics in a Liquid: Optical Activity in Hyper-Rayleigh Scattering from Au Helicoids. *Nano Lett.* **2020**, *20* (8), 5792−5798.
(38) Chen, S.; Reineke, B.; Li, G.; Zentgraf, T.; Zhang, S. Strong Nonlinear Optical Activity Induced by Lattice Surface Modes on Plasmonic Metasurface. *Nano Lett.* **2019**, *19* (9), 6278−6283.
(39) Li, Z. W.; Liu, C. X.; Rong, X.; Luo, Y.; Cheng, H. T.; Zheng, L. H.; Lin, F.; Shen, B.; Gong, Y. J.; Zhang, S.; Fang, Z. Y. Tailoring MoS2 Valley-Polarized Photoluminescence with Super Chiral Near-Field. *Adv. Mater.* **2018**, *30* (34), 1801908.
(40) Collins, J. T.; Hooper, D. C.; Mark, A. G.; Kuppe, C.; Valev, V. K. Second-Harmonic Generation Optical Rotation Solely Attributable to Chirality in Plasmonic Metasurfaces. *ACS Nano* **2018**, *12* (6), 5445−5451.
(41) Li, Z. W.; Li, Y.; Han, T. Y.; Wang, X. L.; Yu, Y.; Tay, B.; Liu, Z.; Fang, Z. Y. Tailoring MoS_2 Exciton-Plasmon Interaction by Optical Spin-Orbit Coupling. *ACS Nano* **2017**, *11* (2), 1165−1171.
(42) Chen, S.; Zeuner, F.; Weismann, M.; Reineke, B.; Li, G.; Valev, V. K.; Cheah, K. W.; Panoiu, N. C.; Zentgraf, T.; Zhang, S. Giant Nonlinear Optical Activity of Achiral Origin in Planar Metasurfaces with Quadratic and Cubic Nonlinearities. *Adv. Mater.* **2016**, *28* (15), 2992−2999.
(43) Kolkowski, R.; Petti, L.; Rippa, M.; Lafargue, C.; Zyss, J. Octupolar Plasmonic Meta-Molecules for Nonlinear Chiral Watermarking at Subwavelength Scale. *Acs Photonics* **2015**, *2* (7), 899−906.
(44) Bertolotti, M.; Belardini, A.; Benedetti, A.; Sibilia, C. Second harmonic circular dichroism by self-assembled metasurfaces [Invited]. *J. Opt. Soc. Am. B* **2015**, *32* (7), 1287−1293.
(45) Valev, V. K.; Baumberg, J. J.; De Clercq, B.; Braz, N.; Zheng, X.; Osley, E. J.; Vandendriessche, S.; Hojeij, M.; Blejean, C.; Mertens, J.; Biris, C. G.; Volskiy, V.; Ameloot, M.; Ekinci, Y.; Vandenbosch, G. A. E.; Warburton, P. A.; Moshchalkov, V. V.; Panoiu, N. C.; Verbiest, T. Nonlinear Superchiral Meta-Surfaces: Tuning Chirality and Disentangling Non-Reciprocity at the Nanoscale. *Adv. Mater.* **2014**, *26* (24), 4074−4081.
(46) Kim, D.; Yu, J.; Hwang, I.; Park, S.; Demmerle, F.; Boehm, G.; Amann, M.-C.; Belkin, M. A.; Lee, J. Giant Nonlinear Circular Dichroism from Intersubband Polaritonic Metasurfaces. *Nano Lett.* **2020**, *20* (11), 8032−8039.
(47) Zhang, S.; Li, G. C.; Chen, Y.; Zhu, X.; Liu, S. D.; Lei, D. Y.; Duan, H. Pronounced Fano Resonance in Single Gold Split Nanodisks with 15 nm Split Gaps for Intensive Second Harmonic Generation. *ACS Nano* **2016**, *10* (12), 11105−11114.
(48) Liu, S. D.; Leong, E. S. P.; Li, G. C.; Hou, Y.; Deng, J.; Teng, J. H.; Lei, D. Y.; et al. Polarization-Independent Multiple Fano Resonances in Plasmonic Nonamers for Multimode-Matching Enhanced Multiband Second-Harmonic Generation. *ACS Nano* **2016**, *10* (1), 1442−1453.
(49) Li, G.-C.; Lei, D.; Qiu, M.; Jin, W.; Lan, S.; Zayats, A. V. Light-induced Symmetry Breaking for Enhancing Second-Harmonic Generation from an Ultrathin Plasmonic Nanocavity. *Nature Communications.* **2021**, *12* (1), 1−8.
(50) Chen, Y.; Yang, X.; Gao, J. Spin-Selective Second-Harmonic Vortex Beam Generation with Babinet-Inverted Plasmonic Metasurfaces. *Advanced Optical Materials* **2018**, *6* (19), 1800646.
(51) O'Brien, K.; Suchowski, H.; Rho, J.; Salandrino, A.; Kante, B.; Yin, X.; Zhang, X. Predicting nonlinear properties of metamaterials from the linear response. *Nat. Mater.* **2015**, *14* (4), 379−383.
(52) Hou, Y.; Qiu, M.; Cao, Z.; Zhou, J.; Ong, H. C.; Jin, W.; Du, J.; Lei, D. High-Q Circular Dichroism Resonances in Plasmonic Lattices with Chiral Unit Cells. *Adv. Funct. Mater.* **2022**, *32*, 2204095.

https://doi.org/10.1021/acs.nanolett.2c02283
Nano Lett. XXXX, XXX, XXX−XXX